

UC Berkeley

UC Berkeley Previously Published Works

Title

Crustal structure and upper mantle anisotropy of the Afar triple junction

Permalink

<https://escholarship.org/uc/item/6tf4n3jg>

Journal

Earth, Planets and Space, 73(1)

ISSN

1343-8832

Authors

Kumar, U
Legendre, CP
Huang, BS

Publication Date

2021

DOI

10.1186/s40623-021-01495-0

Copyright Information

This work is made available under the terms of a Creative Commons Attribution License, available at <https://creativecommons.org/licenses/by/4.0/>

Peer reviewed

FULL PAPER

Open Access



Crustal structure and upper mantle anisotropy of the Afar triple junction

U. Kumar¹, C. P. Legendre^{1,2*}  and B. S. Huang¹

Abstract

The Afar region is a tectonically distinct area useful for studying continental break-up and rifting. Various conflicting models have been suggested to explain the lateral variations of the anisotropy in this region. To address this issue, we investigated the tectonics of the Afar region using receiver function and shear-wave splitting measurements based on broadband seismic data from 227 stations in the region. Further, the receiver function results were inverted to obtain the crustal thickness and V_p/V_s ratio of the region. Our results reveal a thick African crust (thicker than 40 km) with typical V_p/V_s values for the continental crust, elongated down to 21 km along the rift system with very high V_p/V_s values near the fractured zones, suggesting crustal thinning near the fractured zones. Our shear-wave splitting measurements indicate a general fast axis orientation of N030E. However, substantial disparities in the fast anisotropy direction exist in the triple junction region, with some stations displaying a direction of N120E, which is perpendicular to the fast directions measured at the surrounding stations. In addition, many stations located close to the rifts and within the Arabian Plate provide mostly null measurements, indicating the presence of fluids or isotropic media. This study uses several methodologies to unravel the structure and evolution of the Afar region, providing valuable insight into the Afar, a tectonically distinct region, which will be useful for elucidating the mechanisms and characteristics of a continental break-up and the rifting process.

Keywords: Afar, Continental break-up, Continental rifting, Crustal structure, Receiver function, Shear-wave splitting

Introduction

Geological settings

The Afar triple junction (Fig. 1) is located in East Africa connecting three branches of a complex rift system. This area is an example of the last stage of continental rifting and the early stage of seafloor spreading, leading to the creation of oceanic crust (Mohr 1970; Tesfaye et al. 2003; Rychert et al. 2012). The Afar hotspot is located at the triple junction between the Red Sea rift, the Gulf of Aden, and the Ethiopian rift zone (Mohr 1970; Legendre 2013). The Red Sea rift is considered as the boundary between the Arabian and African (Nubian) plates, whereas the Gulf of Aden separates the Arabian and African (Somalian) plates (Bird 2003). The Ethiopian rift zone (also

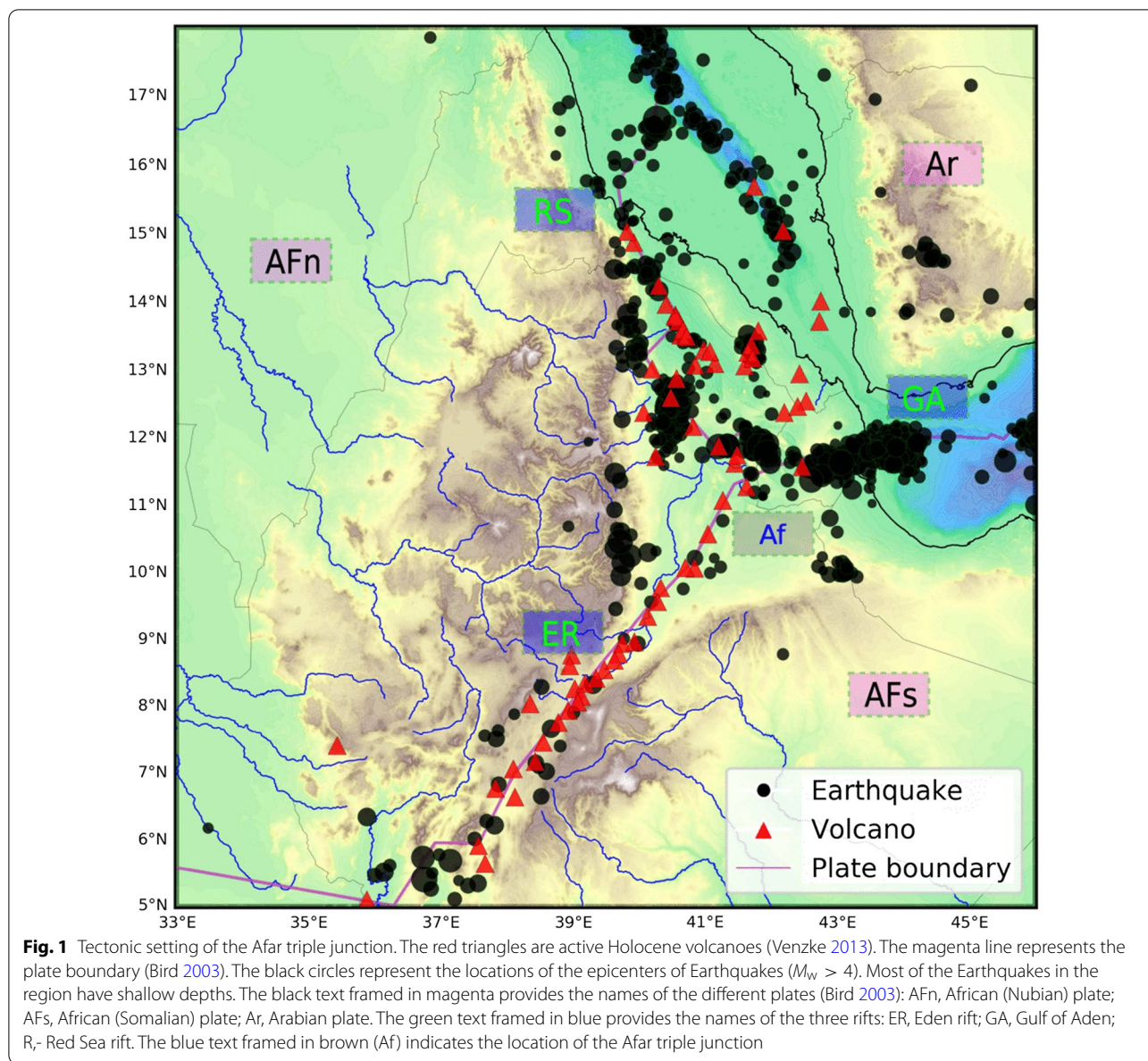
called East African Rift System), an active continental rift zone in East Africa, is a divergent tectonic plate boundary (Kusky et al. 2010) dividing the African Plate into two tectonic units: the Nubian and Somalian plates (Garfunkel and Beyth 2006). The Afar triple junction accommodates the divergent motions between the Arabian, Nubian, and Somalian plates along the Red Sea, Gulf of Aden, and East African rifts. The kinematics of the Afar triple junctions are generally studied using long-term deformation and geodetic observations (McClusky et al. 2010) as well as geodynamical modeling (Koptev et al. 2018).

The opening of the Red Sea and the Gulf of Aden started in the Late Eocene–Early Oligocene (Ghebreab 1998) and led to the split between Africa and Arabia in the Early Miocene (Joffe and Garfunkel 1987). The early stage of the collision between the Mediterranean and Biltis segments (McQuarrie et al. 2003) occurred

*Correspondence: legendre@Earth.sinica.edu.tw

¹ Institute of Earth Sciences, Academia Sinica, Taipei, Taiwan

Full list of author information is available at the end of the article



synchronously with the massive eruption of flood basalt associated with the Afar plume at around 30 Ma (Hofmann et al. 1997).

Previous geophysical studies

Several geophysical tools have been employed in this region to investigate its tectonics. In recent decades, the Global Positioning System (GPS) has been widely deployed in this region to investigate the relative motions of the different tectonic units (Walpersdorf et al. 1999; McClusky et al. 2010; Doubre et al. 2017).

The main results of geodetic measurements along the Afar triple junction have suggested counterclockwise

rotation with respect to the Nubian Plate (with a rotation pole located in the central Red Sea). Doubre et al. (2017), based on a combination of GPS and Interferometric Synthetic Aperture Radar (InSAR) measurements, suggested that the northern part of the Somalia plate evolves independently from the entire African (Somalian) plate.

Previous seismological models from body-wave tomography (Benoit et al. 2006; Koulakov 2007) and surface-wave tomography (Sebai et al. 2006; Guidarelli et al. 2011; Legendre 2013) corroborated the presence of negative velocity anomalies beneath the triple rift systems. Also, they have suggested that the Afar hotspot and other volcanic provinces in the region (Wignall 2001; Mège and

Korme 2004) are originating from the African superplume (Ni et al. 2002; Simmons et al. 2007), upwelling from the lower mantle.

The crustal thickness in the region is of great interest as it is crucial to unraveling the mechanisms of the tectonic evolution of the Afar triple junction. The Moho depth has been widely investigated using the receiver function technique (Dugda et al. 2005; Dugda and Nyblade 2006; Hammond et al. 2011; Reed et al. 2014; Thompson et al. 2015) and the crustal thickness ranges from ~ 15 km beneath the spreading centers up to ~ 40 – 45 km outside the continental break-up area (Hammond et al. 2011).

Previous anisotropy observations have mainly been achieved by the shear-wave splitting of teleseismic (Gashawbeza et al. 2004; Walker et al. 2005) or local Earthquakes (Keir et al. 2011). Several other shear-wave splitting measurements performed in the region and surroundings have been compiled into international shear-wave splitting databases (Wüstefeld et al. 2009; IRIS 2012). Deformation-related structures generally explain the anisotropic pattern in the Afar region. The general orientation of the anisotropies is associated with mantle flow; in contrast, subtle changes in the fast direction are related to the presence of fluids, isotropic media, or vertical mantle flow. Dyke-induced faulting and alignment of melt pockets near volcanic centers also have very distinct anisotropic patterns in the region (Gashawbeza et al. 2004).

Tectonics of the Afar triple junction

The tectonics of the Afar triple junction is dominated by the motion of three plates: Arabia, Africa (Nubia), and Africa (Somalia). The first rift to open is thought to have been the Gulf of Aden around 30 Ma (Ghebreab 1998). Simultaneously, the intense activity of the Afar hot-spot (Schilling et al. 1992; Hofmann et al. 1997) led to a massive amount of flood basalt in the region. The opening of the Red Sea rift (Kusky et al. 2010) is thought to have started between 24 and 21 Ma. This event was followed by high magnetic anomalies (Wignall 2001; Mège and Korme 2004) and subsequently the opening of the Ethiopian rift between 18 and 15 Ma (Kusky et al. 2010). The local seismicity (Abdallah et al. 1979; Illsley-Kemp et al. 2018), surface displacement (Walpersdorf et al. 1999; Kusky et al. 2010) and geometry of the active faults (Dobre et al. 2017) were used to fine-tune the geometry and complexity of the tectonic units interacting in the region. Further information from body-wave tomography (Benoit et al. 2006) and surface-wave tomography (Guidarelli et al. 2011), as well as receiver function results (Hammond et al. 2011), have provided additional constraints on the nature of these tectonic units, such as their lateral and vertical extensions and the presence of

rigid blocks in the region. Further geophysical modeling (Simmons et al. 2007; Reilinger and McClusky 2011) has enabled the kinematics and dynamics of the region to be refined. However, conflicting models have been suggested to explain the lateral variations of the anisotropy in the Afar triple junction region. Gao et al. (2010) suggested that the optimal source of anisotropy is located at approximately 300 km depth (in the asthenosphere), whereas Keir et al. (2011) found that this anisotropy originates mostly from deformation-related structures in the crust and lithosphere.

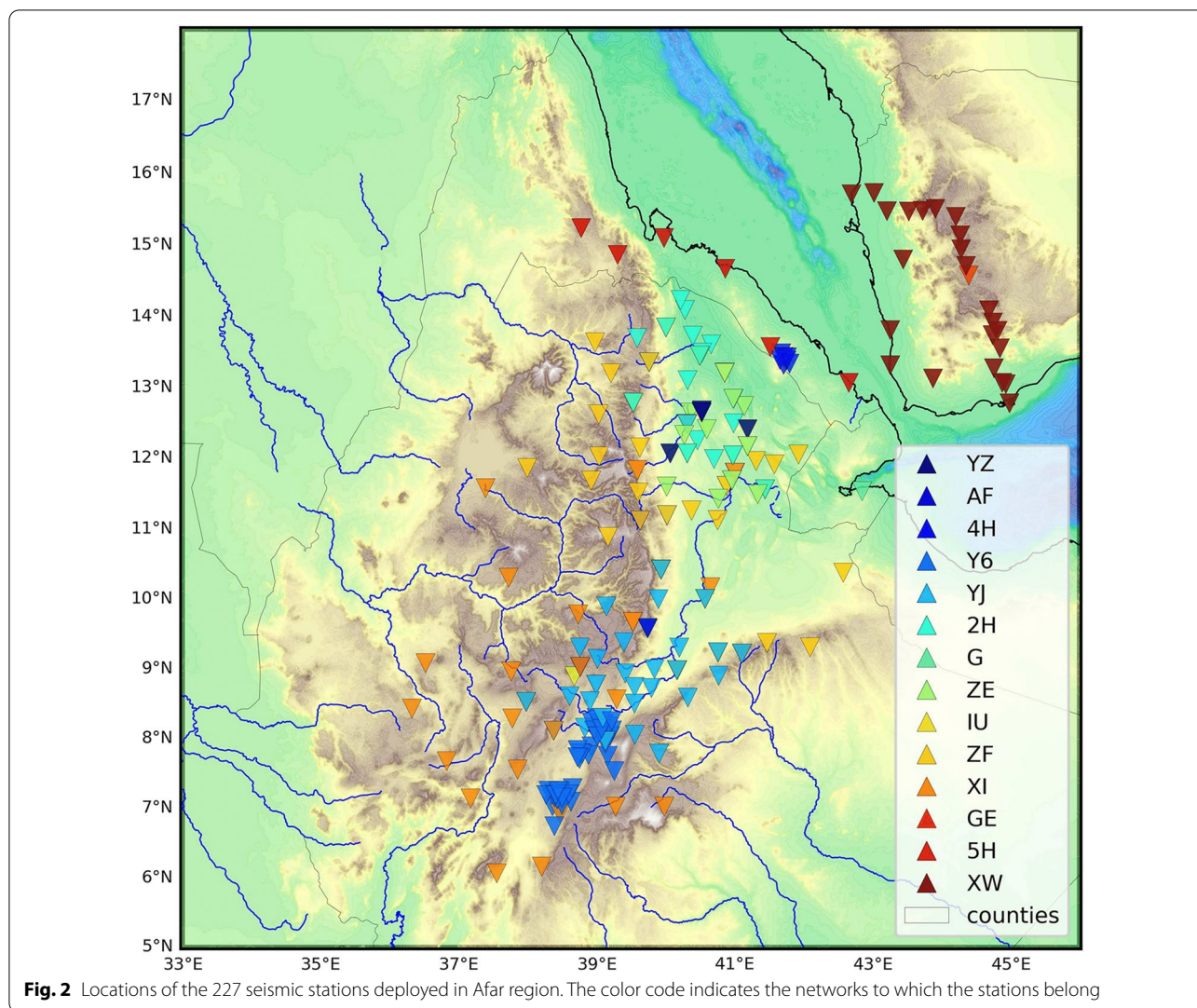
In this study, we performed a systematic investigation of the crustal structure and mantle anisotropy in the Afar region by means of receiver function and shear-wave splitting analyzes. Knowledge about the crustal thickness as well as crustal and lithospheric anisotropies (Legendre et al. 2017, 2020) can provide helpful insight into the crustal and mantle flow affecting the regional dynamics (Legendre et al. 2016; Fan et al. 2020). The main contribution of this study is a total of 431 new shear-wave splitting measurements in the region as well as 34 measurements of crustal thickness and ratio of seismic compressional and shear-wave velocities (V_p/V_s). In the first step, we will describe the data and methodologies used in this study (“Data and methods”). “Results” presents our new findings based on crustal thickness, velocity ratio between compressional waves and shear waves as well as shear-wave splitting of the SKS phase. “Discussion” discusses the implications of our computed crustal depth, $\frac{V_p}{V_s}$ ratio, and anisotropy in terms of the structures, composition, and evolution of local and regional features.

Data and methods

Seismological data

We searched for all available broadband seismic stations deployed in the study region (Fig. 2). In total, 227 stations were found, but only 223 used for receiver functions and 224 used for shear-wave splitting constraints provided sufficient data for further investigation. To compute the receiver functions, we selected each available Earthquake with $M_w > 5.5$ and an epicentral distance between 30° and 90° , and to perform the shear-wave splitting measurements at each station, we selected Earthquakes with $M_w > 6.5$ with epicentral distances ranging from 90° to 120° .

We selected the accessible Earthquakes independently for each station. The number of Earthquakes mainly varies with the station operating time. We selected 427 events among all stations to compute the receiver functions and 514 for the shear-wave splitting measurements. Waveform data were downloaded from global open-access data centers (mostly from the GEOForschungsNetz program (GEOFON), GeoForschungsZentrum Potsdam, Observatories and Research Facilities for



European Seismology Data Center and Incorporated Research Institutions for Seismology Data Management Center) (Megies et al. 2011; Trabant et al. 2012).

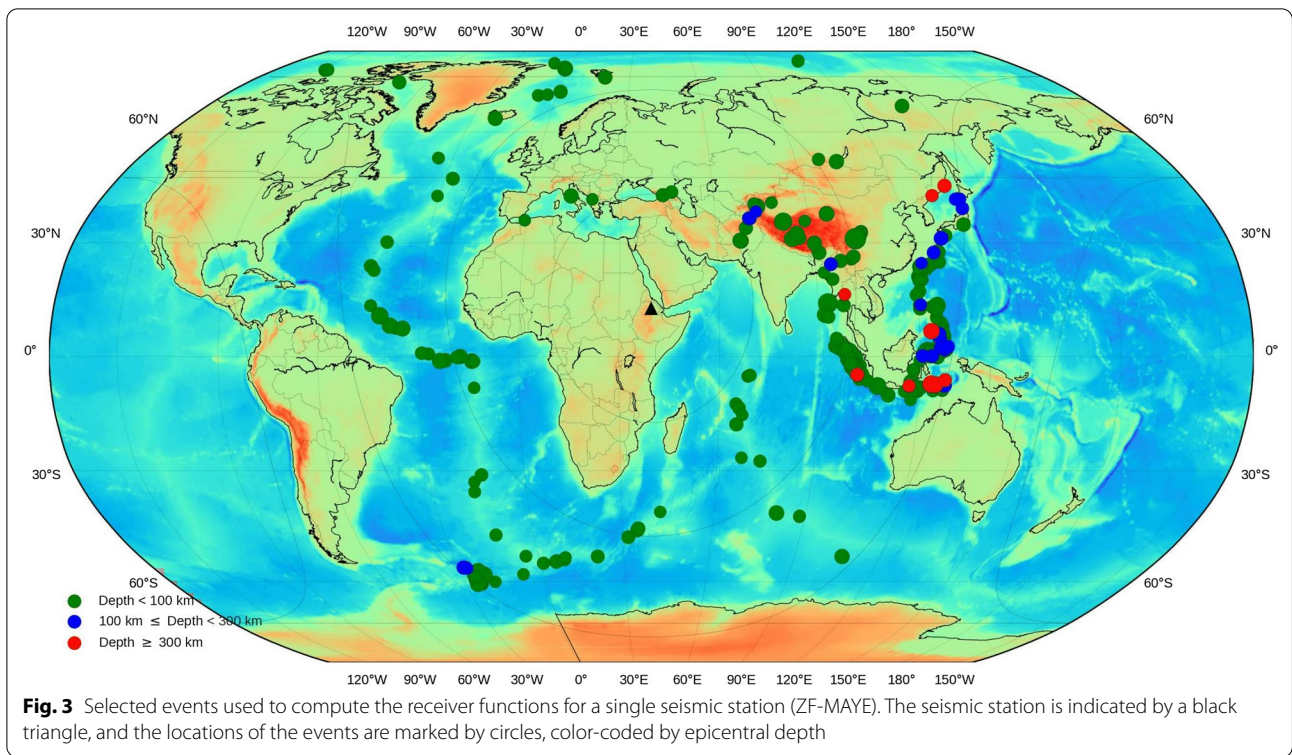
Receiver functions

Receiver functions are time series representing the internal boundaries of the Earth near the receiver, converting the incident P waves into S waves, or vice versa. The receiver function method is well established and widely used to investigate crustal and upper mantle velocity discontinuities (Langston 1979; Ammon et al. 1990; Zhu and Kanamori 2000; Kind et al. 2015; Maguire et al. 2018).

Herein, we illustrate the method implemented by Eulenfeld (2020) using a single station, ZF-MAYE. Figure 3 summarizes the potential events selected for this station and satisfying the magnitude and epicentral distance requirements.

The ZRT coordinates (vertical, radial, and transverse components) were conveniently adopted for the nearly vertical incidence of teleseismic events. Assuming the location of the station–hypocenter pair is known, it is possible to infer the wave coordinate system. The L component is associated with the P-wave polarization, whereas the Q component is tied to S_V -wave polarization, and the T component is related to the S_H -wave polarization.

In this study, the particle motions of the incident and converted waves were separated using the wave coordinates. To derive the P-receiver functions, the teleseismic waveform of the L (or Z) component (assumed to resemble that of a P wave striking the conversion boundary) is deconvolved from the QT (or RT) components to separate the source effects of the converted phases. The resulting receiver function (the Q component in particular) reveals the delay time (relative to the P-wave onset)



and relative amplitudes of the P waves converted into S waves (Ps) by the significant discontinuity, as well as multiples (PpP_{mP}, PpS_{mP}, PpP_{mS}, and PpS_{mS}) caused by reverberations within the layer. P indicates a P-wave in the mantle, p indicates a P-wave ascending to the surface, S indicates an S-wave in the mantle, s indicates an S-wave ascending to the surface, whereas m indicates a top-side reflection from the Moho.

Those phases are not easily identified on a seismogram, because they generally have low amplitude and are hidden in the coda of teleseismic P-wave coda. A conventional approach is to build the receiver function, and to highlight those compressional motion converted into shear-polarized motion. The underlying assumption is that the vertical component is primarily related to the compressional motion. Thus, deconvolving it from the horizontal components removes the signature of the Earthquake source (present in both horizontal and vertical components of the seismogram), as well as all compressional reverberations. The resulting product of the deconvolution is the time series of shear motion within the teleseismic P-wave coda. More details about the deconvolution process are available at Walpole et al. (2014) and Kumar and Legendre (2021).

The horizontal components of the seismogram are rotated into LQT components (L is aligned in the direction of P wave propagation; Q is aligned in the direction

of the S_v phase movement whereas T is aligned in the direction of the S_H phase movement).

The L and Q receiver functions are obtained by deconvolving the vertical component seismogram of a single teleseismic event from the L and Q components seismogram, respectively, using the time domain source equalization method of Langston (1979), as shown in Eq. (1):

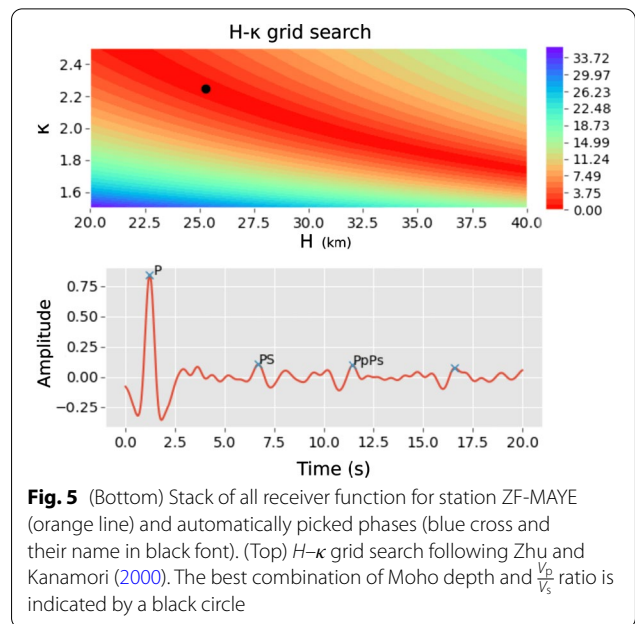
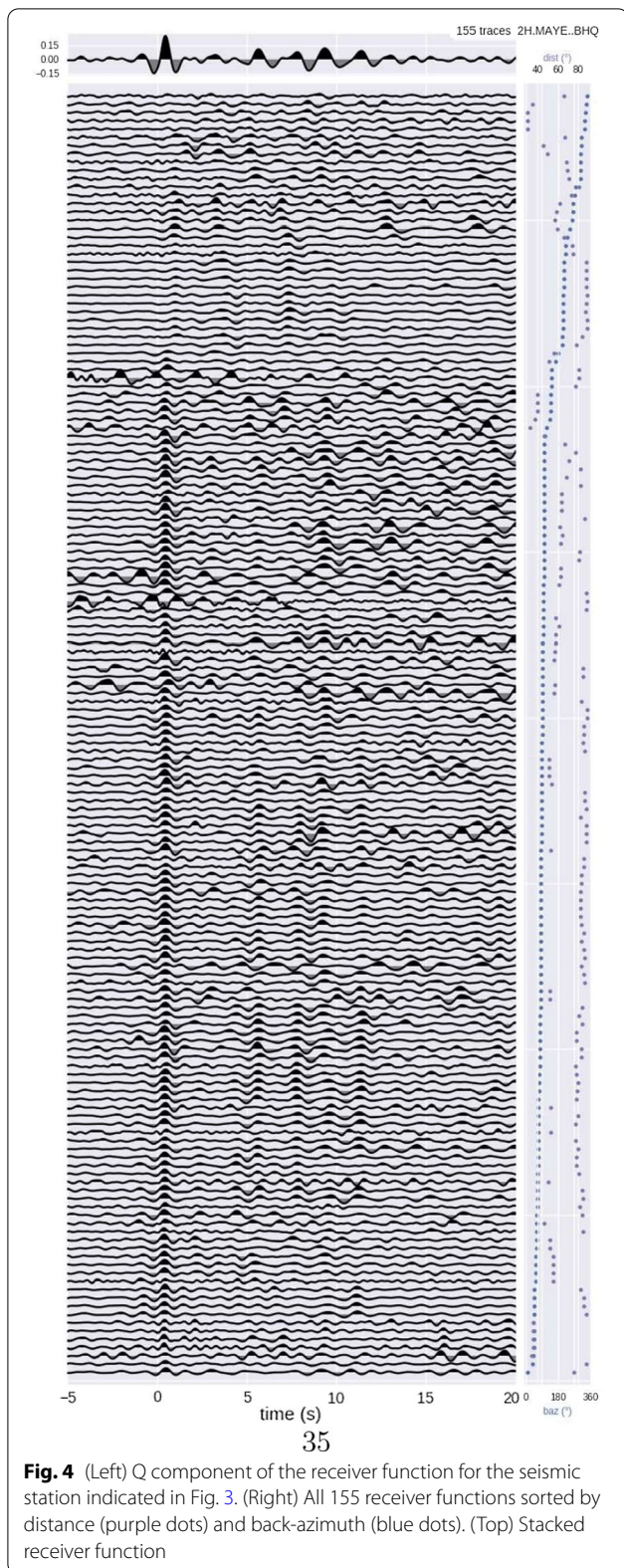
$$RF_L(\omega) = c(\omega) \cdot \frac{L(\omega)}{Z(\omega)},$$

$$RF_Q(\omega) = c(\omega) \cdot \frac{Q(\omega)}{Z(\omega)}. \tag{1}$$

Figure 4 displays the receiver functions computed at the selected station (ZF-MAYE).

H-κ stacking

We stacked all receiver functions that were reasonable for each station to produce an average receiver function for that station (Fig. 4, top). Stacking receiver functions enhances the signal-to-noise ratio of the trace, thereby increasing the amplitude of the converted phases in the receiver function. Theoretically, all converted phases should be visible on the stacked receiver function. However, some converted phases have very low amplitudes and are not easy to discriminate.



To ensure the reliability of the $H-\kappa$ stack, we selected only the receiver functions that were of high quality and discarded those with more uncertainty. In a first step, we discarded all receiver functions that had a signal-to-noise ratio lower than 3. Only the receiver functions with clear direct P, PS, and P_pP_s phases were retained. We used an automated tool (Eulendorf 2020; Kumar and Legendre 2021) to identify the potential phases in the stacked seismogram (Fig. 5, bottom) where only the phases with strong amplitude contrasts were easily recognized. We set the first peak with the highest amplitude as the direct P-wave arrival. The first peak with an amplitude more significant than 10% of the P-wave arrival amplitude was considered to correspond to the P-to-S converted (PS) wave. The second peak with an amplitude greater than 5% of the P-wave arrival amplitude was considered the P_pP_s wave.

The conventional $H-\kappa$ stacking method (Zhu and Kanamori 2000) requires another phase: the P_pS_s or P_sP_s that arrive 15–20 s after the direct P arrival. However, this phase has a negative amplitude and was not always picked by our automated picking method. Therefore, we only use those three arrival times to constrain the Moho depth (H) as well as the $\frac{V_p}{V_s}$ ratio (κ), following:

$$H = \frac{(t_1 - t_0)}{\sqrt{(\frac{\kappa}{V_p})^2 - p^2} - \sqrt{(\frac{1}{V_p})^2 - p^2}},$$

$$H = \frac{(t_2 - t_0)}{\sqrt{(\frac{\kappa}{V_p})^2 - p^2} - \sqrt{(\frac{1}{V_p})^2 - p^2}},$$

(2)

where t_0 is the arrival time of the P wave, t_1 is the arrival time of the PS wave, t_2 is the arrival time of the P_pP_s wave, V_p is set to 6.3 km/s (based on the IASP91 reference model from Kennett et al. (1995), κ is the $\frac{V_p}{V_s}$ ratio. H is the Moho depth (in km). A 65% weight was given to the PS arrival time in Eq. (2) and 35% was given to the P_pP_s arrival time, following Zhu and Kanamori (2000). Note that the calculated crustal thickness is strongly influenced by the initial velocity model, which is also affected by the thickness of the sedimentary layer.

For each station where the stacked receiver function displayed enough amplitude on the selected phases, both Moho depth (H) and $\frac{V_p}{V_s}$ ratio (κ) could be retrieved, as displayed in Fig. 10.

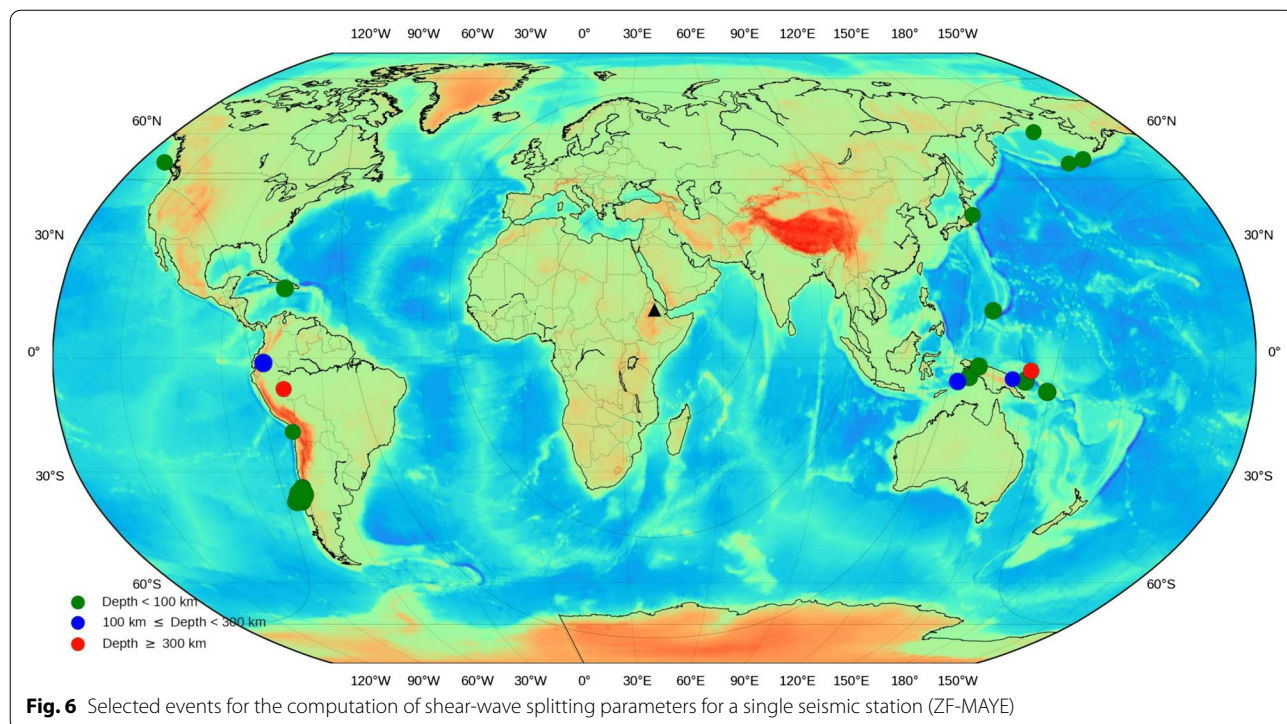
Some receiver functions failed to provide enough energy at the predicted arrival times for the P_pP_s phase due to the instability of the deconvolution (Kind et al. 2015). Of the 223 seismic stations that provided data for receiver function inversion, 34 also supplied measurements for the $H-\kappa$ stacking method (Zhu and Kanamori 2000). Most stations provided receiver functions results, but we imposed highly restrictive quality checks to ensure that the $H-\kappa$ stacking method would yield consistent results. The quality checks consist of two steps: first, the receiver function requires a signal-to-noise ratio higher than 3. Then all the phases used for the $H-\kappa$ stacking method need to be consistently determined for each station specific stacked receiver function.

Shear-wave splitting

Shear-wave polarization anisotropy from core phases is a well-established concept (Ando et al. 1983; Fukao 1984; Obrebski et al. 2010). To download and process the data, we followed the workflow of STADIUM-py (Walpole et al. 2014).

For each seismic event that matches the magnitude and epicentral distance requirements (Fig. 6), ZNE raw data were downloaded and rotated from ZNE to ZRT components. The predicted arrival time of the SKS phase was calculated using the IASP91 reference model (Kennett et al. 1995). The traces were cut around the SKS phase predicted arrival time (from 30 s before to 45 s after the predicted time), as displayed in Fig. 7.

We then used an automatic selection approach to identify the beginning and ending times of the SKS wave on the radial component (Fig. 8). Characteristic functions calculated using short-term-average/long-term-average (STA/LTA) algorithms are often employed for automated detection of P and S waves and arrival time estimation (Walpole et al. 2014). This study used an automatic selection method based on an STA/LTA algorithm to determine the SKS arrival time accurately. Two threshold values in the characteristic function were set to pick the beginning and end times of the SKS wave accurately (Walpole et al. 2014): the first threshold was for the beginning of the SKS phase,



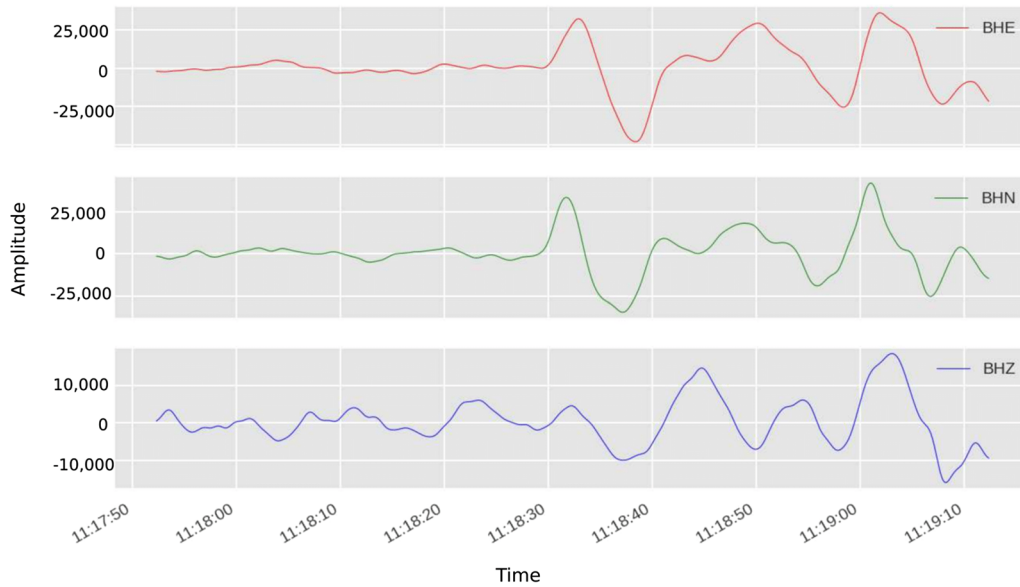


Fig. 7 Raw waveforms of unfiltered ZNE components for an event recorded at station ZF-MAYE (8/9/2009, 10:55:56.28, epicenter (33.1474, 138.0594), epicentral depth of 302.2 km, and $M_w = 7.1$

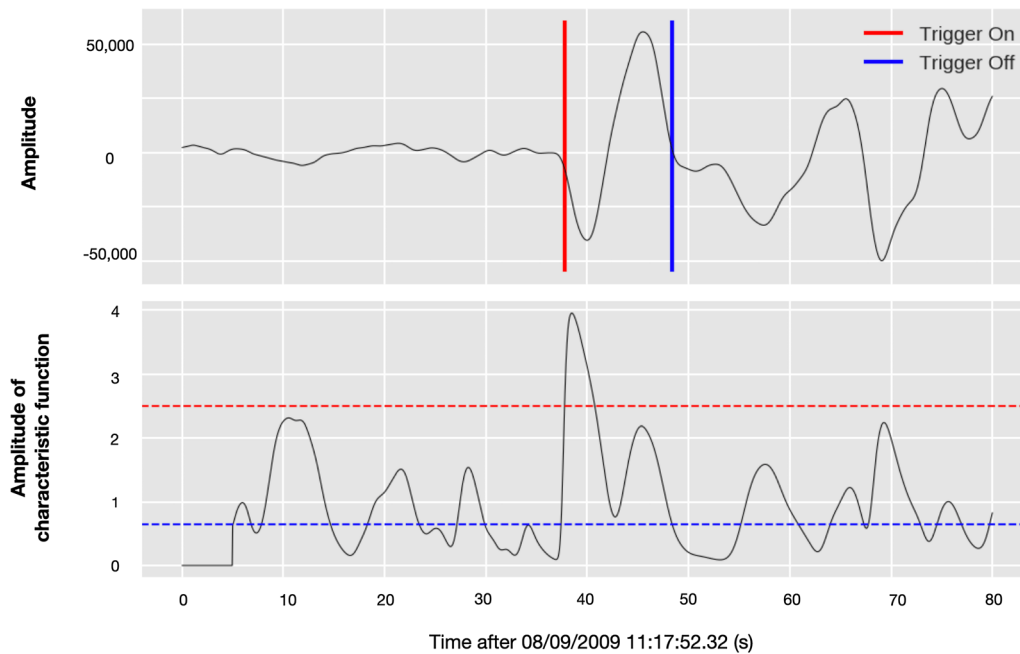
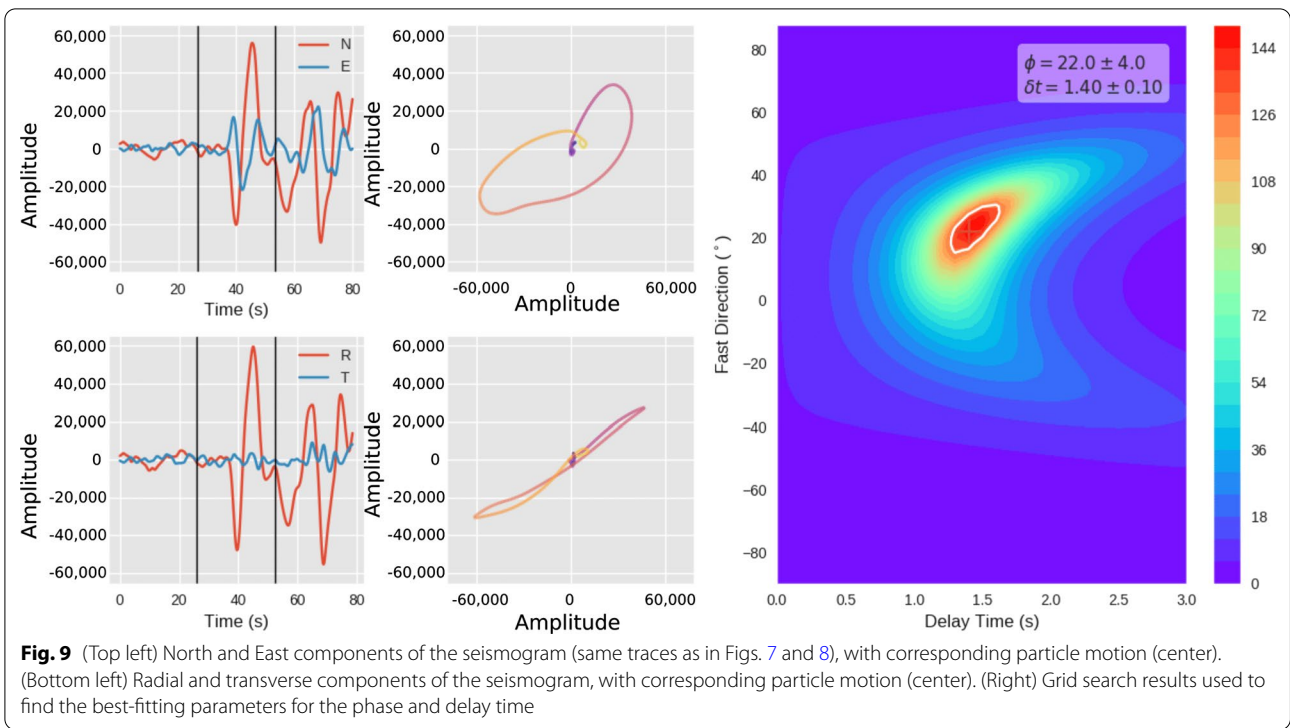


Fig. 8 Automatic selection of the SKS phase using the recursive STA LTA method for the trace depicted in Fig. 7. The red and blue bars indicate the beginning and ending times of the SKS phase, based on values of the characteristic function (bottom)

and the second was for the end of the SKS phase (red and blue lines in Fig. 8, respectively).

Once the SKS phase had been selected, we performed a grid search (Fig. 9) for the best-fitting splitting parameters following (Walpole et al. 2014). To pass the grid

search successfully, we set some thresholds on the errors in the phase ($\delta\phi$) and the delay time (δt). Measurements with excessive uncertainties in the fast directions ($\delta\phi > 7^\circ$) and the delay time ($\delta t > 1.5s$) were also discarded. Those threshold values in the phase ($\delta\phi$) and



the delay time (δt) are quite conservative and ensure that the final measurements do not include too many uncertainties.

This grid search (Fig. 9) yielded the fast shear phase (ϕ) and a delay time (δt). The procedure was repeated at each station and for all respective events. In the end, the average of all the measurements was computed at each station.

Results

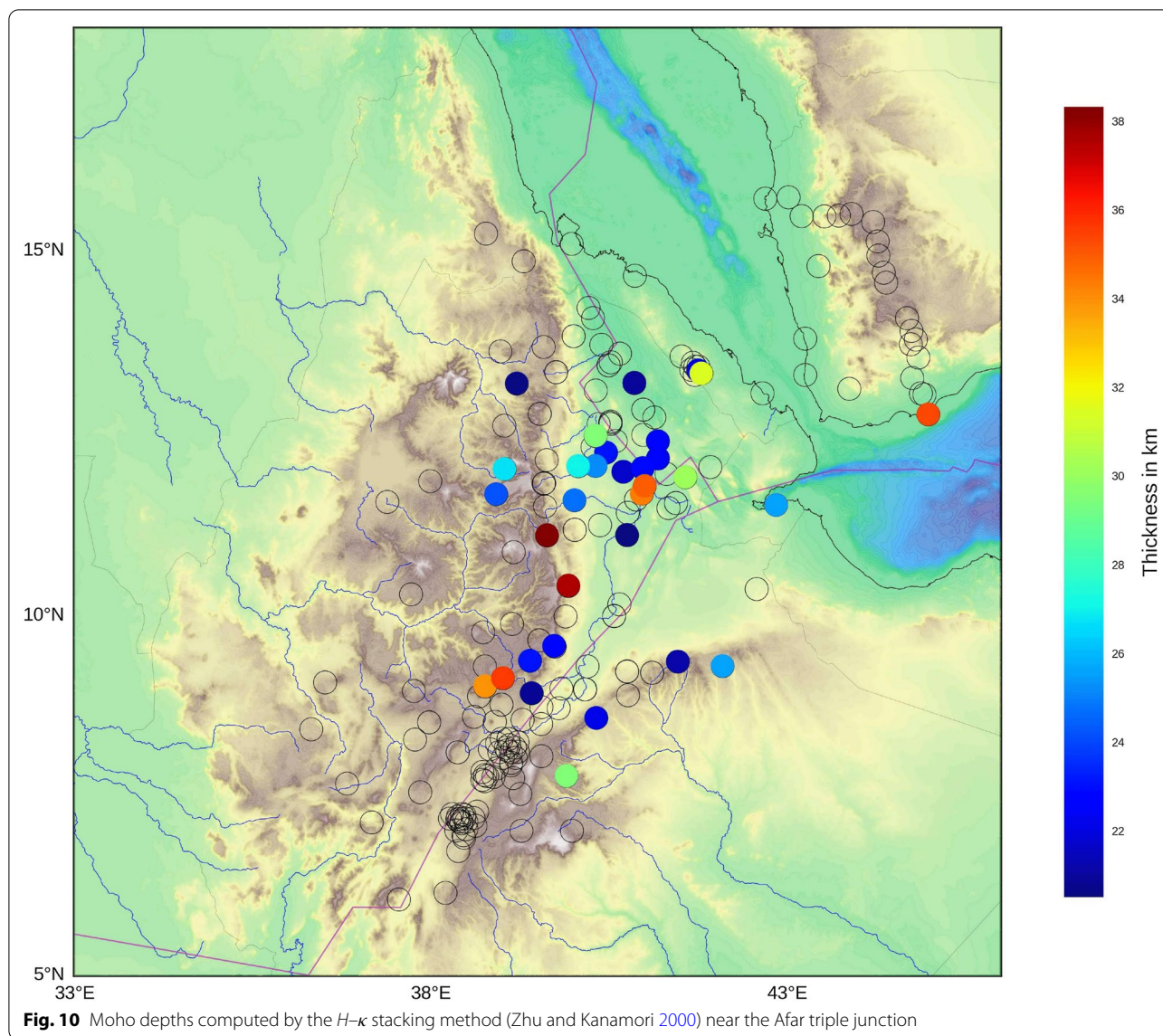
We obtained successful measurements of H and κ for a total of 34 stations. Figures 10 and 11 display the receiver function inversions for H and κ , respectively. Our results suggest that regional thick continental crust (with a thickness of up to 38 km) exists beneath the African and Arabian plates, which agrees with previous measurements (Dugda et al. 2005; Dugda and Nyblade 2006; Hammond et al. 2011; Reed et al. 2014; Thompson et al. 2015). In contrast, a very thin crust (with a thickness as low as 21 km) is found along the three branches of the continental rifting and beneath the Afar triple junction. This thin crust is consistent with the very thin crustal thickness found beneath the spreading centers and the area of continental break-up (Hammond et al. 2011). Hammond et al. (2011) found that the crustal thickness ranged from 16 km down the spreading centers in the northern Afar region to

20–25 km near the active rift segments and observed a northward thinning of the crust beneath the Afar triple junction.

$\frac{V_p}{V_s}$ ratio is expected to be in the range 1.7–1.9 in the continental crust (Zandt and Ammon 1995; Musacchio et al. 1997; Kandilarov et al. 2015); most of the measurements in the region (Fig. 11), the value of $\frac{V_p}{V_s}$ is reasonable. However, the measurements observed near the continental rift display relatively high values (greater than 2.0). Note that the receiver function results are not displayed for all stations, as their main primary purpose was to compute H and κ using the H - κ stacking method (Zhu and Kanamori 2000).

Figure 12 summarizes the shear-wave splitting measurements, and Table 1 lists them in detail. In most of the regions on the Nubian and Somalian plates, the fast direction is oriented N030E. This fast direction orientation is highly consistent with previous shear-wave splitting measurements (Wüstefeld et al. 2009; IRIS 2012). Along with some additional measurements, we provide detailed information by classifying our results into three categories:

- no data, unreliable measurements (due to insufficient operation time),
- new measurements computed in this study,
- and Null measurements (if number of Null measurements (Wüstefeld and Bokermann 2007) was



more significant than the number of regular measurements).

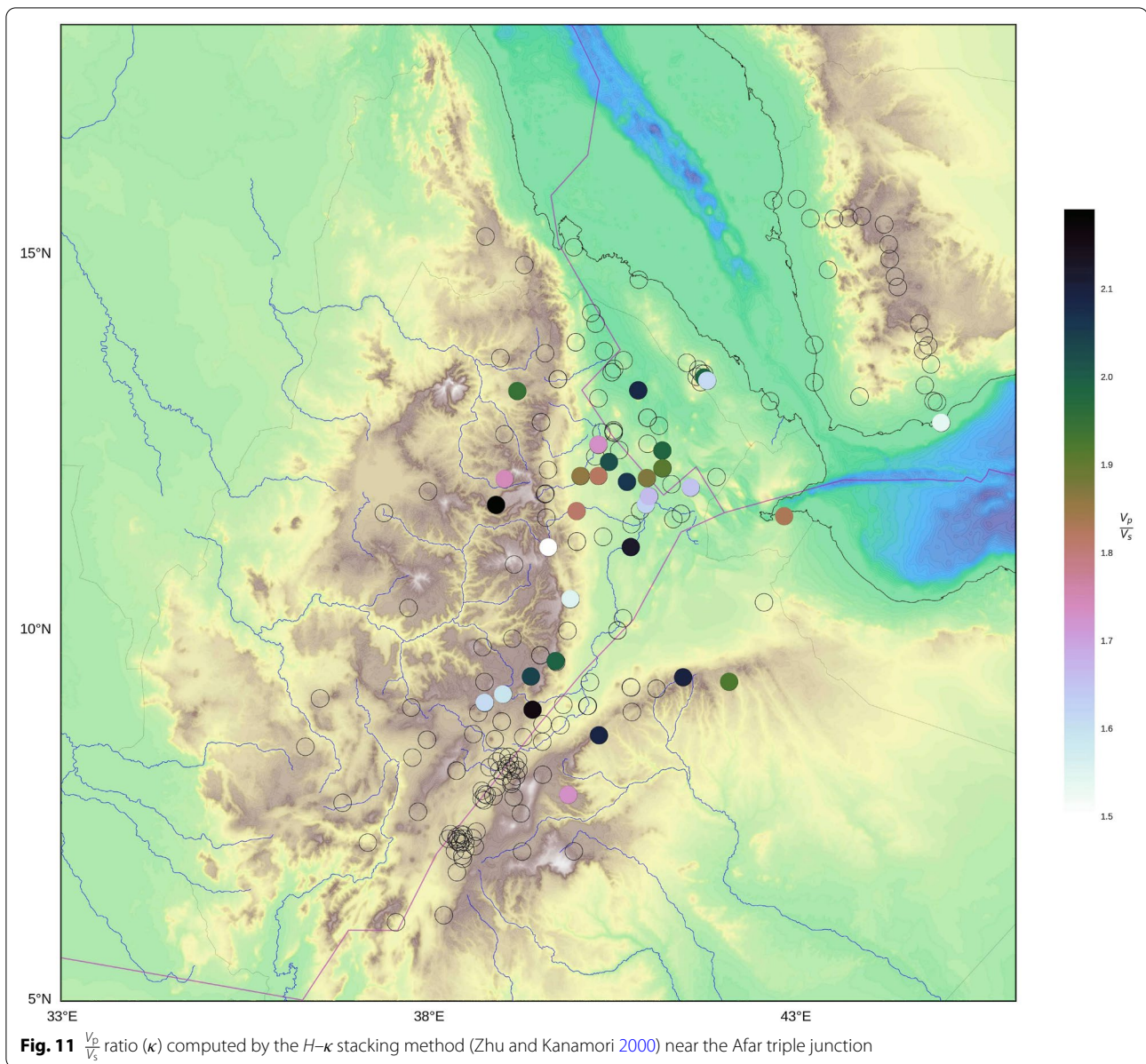
Null measurements can occur for several reasons, such as limited data coverage and azimuthal distribution of seismic events. They can also occur if the wave propagates through an isotropic medium, if the wave encounters fluid, if mantle upwelling occurs with a vertical flow of peridotite, or if the initial polarization direction is oriented along either the fast or slow axis. As the incoming shear wave is not split (Savage 1999), it is not possible to determine or accurately. However, in the central part of the rift, there are several stations with fast directions perpendicular to those of the others, at N120E. For several stations, we could only retrieve null

measurements or no measurements (e.g., beneath the Arabian Plate), which contrasts with the high scattering present in previous measurements (Wüstefeld et al. 2009; IRIS 2012). In the null measurements, we do not report any direction of (ϕ) or (δt) in the station summary (Table 1).

Discussion

Lateral variations of Moho depth

The results we obtained by inverting the Moho depth receiver functions (Fig. 10) agree well with previous measurements (Dugda et al. 2005; Dugda and Nyblade 2006; Hammond et al. 2011; Reed et al. 2014; Thompson et al. 2015). A thick African crust (40–45 km) is

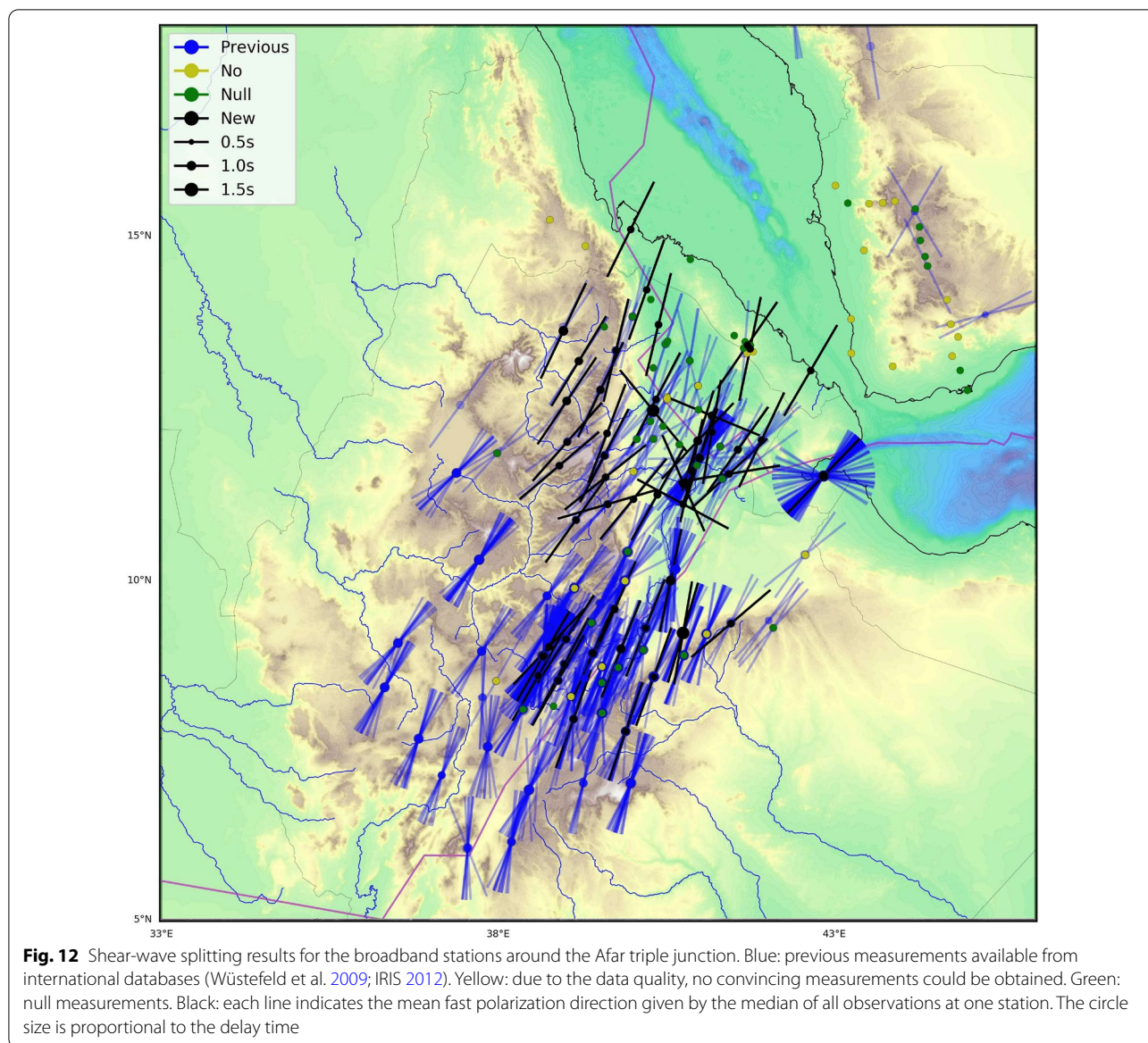


observed near the large igneous volcanic provinces (Wignall 2001; Mège and Korme 2004) beneath the stations located in the continental crust of the Nubian and Somalian plates. These results contrast strongly with the Moho depths we found along the rifts, with a crustal thickness of 21–25 km. This strong dichotomy between the unaltered continental crust and the continental crust thinned by the active continental rifting (Kusky et al. 2010) confirms the theory of the African Plate being split into two tectonic units: the Nubian and Somalian plates (Garfunkel and Beyth 2006).

$\frac{V_p}{V_s}$ ratio reveals the presence of fluids

$\frac{V_p}{V_s}$ ratio has been the topic of numerous studies in oceanic (Clague and Straley 1977; Hyndman 1979; Bloch et al. 2016), continental (Zandt and Ammon 1995; Musacchio et al. 1997; He et al. 2014), and passive margin domains (Kodaira et al. 1996; Kandilarov et al. 2015). Generally, $\frac{V_p}{V_s}$ has been in the range of 1.7–1.9 for the continental crust.

These values agree well with the results obtained for the stations located far away from the rift system (Fig. 11).



However, $\frac{V_p}{V_s}$ increases drastically in the regions affected by active rifting (reaching 2.1, as high as the values found for oceanic domains). This strong contrast of between the unaltered continental crust and thinned crust regions is highly consistent with the mechanical extension of the continental thickness imaged by receiver functions (Fig. 10). The anomalously high $\frac{V_p}{V_s}$, possibly caused by the reduction in shear-velocity (V_s), can be plausible indirect evidence for fluids, melts, or oceanic crust within the rift system branches.

Complex anisotropy beneath the rift system

Previous shear-wave splitting measurements (Wüstefeld et al. 2009; IRIS 2012) display a constant direction of the

fast anisotropy axis throughout the African plate. However, some scattered measurements exist, mainly beneath the Arabian Plate. Our results (Fig. 12) display a similar trend for the stations located on both sides of the rift system beneath the African plates. However, beneath the Arabian Plate, the stations with reliable measurements show null measurements. This null identification suggests that the Arabian block could be isotropic, as it has not experienced substantial deformation since its formation. It is considered a substantially rigid block with limited internal deformation (Allothman et al. 2016; Tesaro et al. 2018) which is consistent with our results. In addition, the high level of inconsistency observed beneath the Arabian plate between the present results and previous

Table 1 Summary of all shear-wave splitting parameters measured in this study for the Afar triple junction region

NET	STA	Long.	Lat.	ϕ	δt	nb	nb Null
2H	ABAE	39.7636	13.3535	14	0	1	3
2H	AFME	40.8585	13.2040	–	–	0	3
2H	AHME	40.2784	14.0889	–	–	0	3
2H	ASYE	41.4422	11.5607	48	0.7	1	4
2H	BTIE	40.0218	11.1949	–	–	0	1
2H	DALE	40.2178	14.2290	20	0.1	1	1
2H	DAME	40.9625	11.6868	–	–	0	1
2H	ERTE	40.4969	13.4463	–	–	0	5
2H	GALE	40.3940	13.7251	14	1.1	2	3
2H	GPSE	40.5283	13.4882	–	–	0	7
2H	GULE	39.5885	13.6945	–	–	0	2
2H	HITE	40.3169	13.1012	–	–	0	1
2H	IGRE	40.4612	12.2526	–	–	0	1
2H	KOZE	40.9849	12.4948	–	–	0	2
2H	LULE	40.7037	11.9892	–	–	0	2
2H	MAYE	39.5343	12.7832	–	–	0	2
2H	SAHE	40.9770	12.0402	17.95	1.5	6	2
2H	SEME	41.0043	11.7926	20.45	1.1	3	4
2H	TRUE	40.3148	12.4812	-40	3	1	3
4H	NAB1	41.6554	13.3873	–	–	0	2
4H	NAB2	41.7146	13.4285	35.39	0.5	3	4
4H	NAB3	41.7549	13.3759	12	0.3	1	1
4H	NAB4	41.6786	13.4788	–	–	0	1
4H	NAB7	41.7562	13.4256	–	–	0	2
5H	ASSE	42.6545	13.0628	31	1	2	2
5H	DOLE	39.9806	15.0968	27	0.9	2	4
5H	FAME	41.5196	13.5684	–	–	0	2
5H	TIOE	40.8666	14.6651	–	–	0	3
AF	AAUS	38.7665	9.03490	43.61	0.9	5	10
AF	ANKE	39.7418	9.58270	24	1.2	2	3
AF	DESE	39.6350	11.1180	74	0.6	1	21
G	ATD	42.8466	11.5307	44.73	1.5	20	18
GE	DAMY	44.3917	14.5725	–	–	0	8
IU	FURI	38.6798	8.89520	30.68	1.2	7	31
XW	ADEN	44.9824	12.7759	–	–	0	3
XW	ANID	43.2048	15.4736	–	–	0	2
XW	DABI	44.2690	15.1325	–	–	0	2
XW	HOTA	44.8757	13.0639	–	–	0	1
XW	RUSA	44.3539	14.7074	–	–	0	1
XW	SANA	44.2068	15.3926	–	–	0	2
XW	YSLE	44.2816	14.9387	–	–	0	1
YJ	ADEE	39.9068	7.79090	19	1.1	2	1
YJ	ADUE	38.9019	8.54040	30	0.4	2	1
YJ	ANKE	39.7339	9.59270	–	–	0	3
YJ	AREE	39.4188	8.93850	24	1.2	3	0
YJ	ASEE	39.1317	7.97290	20	0.9	1	0
YJ	BEDE	40.7710	8.90860	–	–	0	1
YJ	BUTE	38.3824	8.11700	–	–	0	1
YJ	DIKE	39.5566	8.06270	–	–	0	1

Table 1 (continued)

NET	STA	Long.	Lat.	ϕ	δt	nb	nb Null
YJ	DONE	39.5504	8.50900	–	–	0	1
YJ	DZEE	38.9959	8.78030	28	0.7	1	2
YJ	GEWE	40.5743	10.0060	–	–	0	2
YJ	GTFE	39.8376	9.00340	22	1.5	1	0
YJ	KARE	39.9349	10.4224	–	–	0	1
YJ	KOTE	39.3961	9.38750	–	–	0	2
YJ	LEME	38.6095	8.61150	30	0.5	1	1
YJ	MECE	40.3241	8.59380	20	0.7	1	0
YJ	MEKE	38.8330	8.16230	–	–	0	3
YJ	MELE	40.2008	9.31060	22	0.2	1	4
YJ	MIEE	40.7581	9.24160	17	1.9	2	0
YJ	NURE	39.7956	8.73120	–	–	0	1
YJ	SENE	39.0166	9.14660	33	0.5	2	2
ZE	AFME	40.8585	13.2040	–	–	0	7
ZE	AWEE	40.0719	12.0673	–	–	0	1
ZE	BARE	40.3556	12.6443	28	0.1	1	1
ZE	BERE	41.1886	12.1707	–	–	0	1
ZE	BREE	41.1883	12.1704	10	0.6	1	1
ZE	DIGE	40.2734	12.3279	–	–	0	1
ZE	FINE	40.3160	12.0681	–	–	0	3
ZE	HARE	40.8840	11.6072	12.45	0.4	3	3
ZE	MEGE	41.3381	11.4906	–	–	0	1
ZE	MILE	40.7650	11.4238	-24	1.6	1	4
ZE	SEHE	40.9769	12.0401	44	1.4	1	2
ZE	SEME	41.0044	11.7926	18	1.3	1	3
ZE	SILE	41.1879	12.4070	112	1.4	1	3
ZE	TRUE	40.3161	12.4841	–	–	0	5
ZF	ADTE	40.7570	11.1221	118	0	1	4
ZF	ADYE	38.9811	13.6350	26	1.8	3	5
ZF	AKEE	39.1680	10.8883	36	0.4	1	3
ZF	ASYE	41.4422	11.5607	81	0.6	2	2
ZF	AWSE	40.1700	8.98970	–	–	0	1
ZF	BTIE	40.0218	11.1949	40	0.9	1	3
ZF	DERE	39.6353	11.1179	–	–	0	5
ZF	DICE	41.5737	11.9136	36	1.2	2	4
ZF	ELLE	40.3784	11.2579	30	1.2	1	7
ZF	ERTE	40.4969	13.4463	–	–	0	2
ZF	GASE	38.9211	11.6813	50.33	0.7	5	0
ZF	GEWE	40.5739	10.0045	12	1.7	1	1
ZF	HALE	40.0077	13.8422	–	–	0	1
ZF	HYNE	42.0962	9.31480	–	–	0	3
ZF	KOBE	39.6298	12.1506	21	1.1	2	5
ZF	KORE	39.9344	10.4265	–	–	0	4
ZF	LALE	39.0375	12.0258	42	0.2	2	0
ZF	LYDE	41.9257	12.0546	26	0	1	3
ZF	MAYE	39.5343	12.7832	26	1.2	6	5
ZF	MISE	40.7591	9.23690	10	3	1	2
ZF	QATE	41.4691	9.37530	50	1.1	2	0
ZF	SEKE	39.0334	12.6217	34.67	1.4	3	3

Table 1 (continued)

NET	STA	Long.	Lat.	ϕ	δt	nb	nb Null
ZF	SMRE	39.2111	13.1977	32	1.3	1	4
ZF	SRDE	41.3100	11.9579	–	–	0	2
ZF	WLDE	39.5874	11.8243	28	0.9	1	1
ZF	WUCE	39.6064	11.5116	52	0.9	1	2
ZF	YAYE	37.9965	11.8608	–	–	0	1

The columns are for the network code, station code, longitude and latitude of the station, phase (ϕ), delay time (δt), amount of successful measurements and amount of Null measurements. Directions of (ϕ) and δt are not reported for stations considered to provide mostly null measurements

shear-wave splitting measurements (Wüstefeld et al. 2009; IRIS 2012) displayed in Fig. 12, suggests that the previous measurements in this region were not classified as null, despite the strong angular variations of the fast direction of anisotropy. The highly scattered anisotropy directions measured in previous shear-wave splitting studies strongly suggest the presence of isotropic media beneath the Arabian block.

Close to the triple junction, most of the measurements are oriented N030E and agree with previous measurements. However, we also found a few measurements perpendicular to the general trend of N120E. The measurements of those outliers are mainly located close to the triple junction. Figure 12 also indicates that the stations located near the rifts tend to display null measurements. Most stations with null measurements are located near the active Holocene volcanoes (Fig. 1). Although null measurements are not present in the global database, the presence of null measurements can be an important indicator of the presence of fluid or melt beneath the rift branches.

Implications for local tectonics

In this study, 431 new shear-wave splitting measurements were obtained in the investigated region. The average fast direction measured is consistent with the results of Gao et al. (2010). However, the average delay time we found is smaller than that obtained by Gao et al. (2010), which is close to the global average for continents (1.0 s calculated from Kennett et al. (1995) and Silver (1996). The fact that the average delay time is slightly smaller than the global average for continental crust can be explained by the presence of thinned continental crust in our target region. The presence of several stations displaying null measurements also agrees with the results of Gao et al. (2010). The relatively homogeneous pattern of the splitting observed in the region suggests that the main contributor to the anisotropy has a deep origin, with local variations associated with crustal heterogeneities. The relatively homogeneous pattern of the splitting is also consistent with the model proposed by Barruol and Ismail (2001), involving a NE flow in the asthenosphere.

In addition to the lateral flow of the asthenosphere, mantle upwelling is also responsible for the presence of fluids and melt, which is in agreement with the high amount of null measurements, as well as the very high values observed around the branches of the Afar rift system. Those observations are consistent with those of body wave (Benoit et al. 2006; Koulakov 2007) and surface wave (Sebai et al. 2006; Guidarelli et al. 2011; Legendre 2013) tomographic models. The presence of very slow velocities beneath the Afar region (for the global and regional models) and beneath the three branches of the rift system at all depths suggests the presence of fluids and melt, linked with potential mantle upwelling. Previous tomographic studies focusing on anisotropy on a large scale (Sebai et al. 2006) or local scale (Korostelev et al. 2015; Sicilia et al. 2008) have revealed large regions with surface wave slow anomalies that are associated with magmatism. Along the rift system, very slow velocities anomalies have been found, suggesting the presence of either partial melt or fluids released by cooling magmatic systems. The local seismicity (Abdallah et al. 1979; Illsley-Kemp et al. 2018) is also very shallow, suggesting the presence of shallow reservoirs in the crust along the rift system. In those regions, our results indicate both thinner crust, higher values of $\frac{V_p}{V_s}$, and the presence of null measurements.

Conclusion

In this study, we obtained receiver function and shear-wave splitting measurements for all 227 available broadband seismic stations deployed in the Afar region. The receiver function results provide additional constraints on the crustal thickness and $\frac{V_p}{V_s}$ ratio. The shear-wave splitting measurements provide some constraints on the average anisotropy over a column encompassing the crust and upper mantle beneath the seismic stations. Here, we found that the thick African crust (with a thickness of 40 km) has been strongly elongated and thinned (down to a thickness of 20 km) across the rift system. In addition, the exceptionally high $\frac{V_p}{V_s}$ value within the crust along the rifts and numerous null measurements of shear-wave splitting for stations located near the rifts suggests

the presence of melt and the early stage of oceanization. The results of this study provide essential constraints on the structure of the crust and average anisotropy in the Afar region. However, those measurements are limited by the availability of the seismic station deployed in the region. Besides, those measurements provide a 1D snapshot beneath each seismic station, and further modeling such as tomographic inversion could provide a 2D or 3D view of the region. The strong lateral variations of crustal thickness, V_p and seismic anisotropy suggest a more complex pattern with vertical variations that are not visible from our results. However, this study provides accurate measurements of several geophysical parameters that are directly interpreted in terms of the structure and dynamics of the region.

Acknowledgements

Source code, installation instructions and test input files for STADIUM-Py are freely available for download (Kumar and Legendre 2021).

Authors' contributions

UK, CL and BSH contributed to the design and implementation of the research, to the analysis of the results and to the writing of the manuscript. All authors read and approved the final manuscript.

Funding

This work is funded by the Ministry of Science and Technology under Grants MOST 107-2119-M-001-048; MOST 109-2811-M-001 -608- and MOST 109-2116-M-001 -021 -MY3.

Availability of data and materials

All data used in this paper came from published sources listed in the references.

Declarations

Competing interests

The authors declare no competing interests.

Author details

¹Institute of Earth Sciences, Academia Sinica, Taipei, Taiwan. ²Institute of Geophysics, Czech Academy of Science, Prague, Czech Republic.

Received: 17 May 2021 Accepted: 11 August 2021

Published online: 25 August 2021

References

- Abdallah A, Courtillot V, Kasser M, Le Dain AY, Lépine JC, Robineau B, Ruegg JC, Tapponnier P, Tarantola A (1979) Relevance of Afar seismicity and volcanism to the mechanics of accreting Plate boundaries. *Nature* 282(5734):17–23
- Alothman A, Fernandes R, Bos M, Schillak S, Elsaka B (2016) Angular velocity of Arabian Plate from multi-year analysis of GNSS data. *Arab J Geosci* 9(8):529
- Ammon CJ, Randall GE, Zandt G (1990) On the nonuniqueness of Receiver Function inversions. *J Geophys Res Solid Earth* 95(B10):15,303–15,318
- Ando M, Ishikawa Y, Yamazaki F (1983) Shear wave polarization anisotropy in the upper mantle beneath Honshu, Japan. *J Geophys Res Solid Earth* 88(B7):5850–5864
- Barruol G, Ismail WB (2001) Upper mantle anisotropy beneath the African iris and geoscope stations. *Geophys J Int* 146(2):549–561
- Benoit MH, Nyblade AA, VanDecar JC (2006) Upper mantle P-wave speed variations beneath Ethiopia and the origin of the Afar hotspot. *Geology* 34(5):329–332
- Bird P (2003) An updated digital model of plate boundaries. *Geochem Geophys Geosyst* 4(3):1027
- Bloch W, John T, Kummerow J, Wigger P, Salazar P, Shapiro S (2016) Watching dehydration: transient vein-shaped porosity in the oceanic mantle of the subducting Nazca slab. *EGUGA*, pp EPSC2016–6438
- Clague DA, Straley PF (1977) Petrologic nature of the oceanic Moho. *Geology* 5(3):133–136
- Dobre C, Deprez A, Masson F, Socquet A, Lewi E, Grandin R, Nercessian A, Ulrich P, De Chabaliere JB, Saad I et al (2017) Current deformation in central Afar and triple junction kinematics deduced from GPS and InSAR measurements. *Geophys J Int* 208(2):936–953
- Dugda MT, Nyblade AA (2006) New constraints on crustal structure in eastern Afar from the analysis of receiver functions and surface wave dispersion in Djibouti. *Geol Soc Lond Spec Publ* 259(1):239–251
- Dugda MT, Nyblade AA, Julia J, Langston CA, Ammon CJ, Simiyu S (2005) Crustal structure in Ethiopia and Kenya from receiver function analysis: implications for rift development in eastern Africa. *J Geophys Res Solid Earth* 110(B1):B01303
- Eulenfeld T (2020) rf: Receiver function calculation in seismology. *J Open Sour Softw* 5(48):1808
- Fan X, Chen QF, Legendre C, Guo Z (2020) Intraplate volcanism and regional geodynamics in NE Asia revealed by anisotropic Rayleigh-wave tomography. *Geophys Res Lett* 47(1):e2019GL085623
- Fukao Y (1984) Evidence from core-reflected shear waves for anisotropy in the Earth's mantle. *Nature* 309(5970):695
- Gao SS, Liu KH, Abdelsalam MG (2010) Seismic anisotropy beneath the Afar depression and adjacent areas: implications for mantle flow. *J Geophys Res Solid Earth* 115(B12):B12330
- Garfunkel Z, Beyth M (2006) Constraints on the structural development of Afar imposed by the kinematics of the major surrounding plates. *Geol Soc Lond Spec Publ* 259(1):23–42
- Gashawbeza EM, Klemperer SL, Nyblade AA, Walker KT, Keranen KM (2004) Shear-wave splitting in Ethiopia: precambrian Mantle anisotropy locally modified by Neogene rifting. *Geophys Res Lett* 31(18):L18602
- Ghebreab W (1998) Tectonics of the Red Sea region reassessed. *Earth-Sci Rev* 45(1–2):1–44
- Guidarelli M, Stuart G, Hammond JO, Kendall J, Ayele A, Belachew M (2011) Surface wave tomography across Afar, Ethiopia: crustal structure at a rift triple-junction zone. *Geophys Res Lett* 38(24):L24313
- Hammond JO, Kendall JM, Stuart G, Keir D, Ebinger C, Ayele A, Belachew M (2011) The nature of the crust beneath the Afar triple junction: evidence from receiver functions. *Geochem Geophys Geosyst* 12(12):Q12004
- He R, Shang X, Yu C, Zhang H, Van der Hilst RD (2014) A unified map of Moho depth and V_p/V_s ratio of continental China by receiver function analysis. *Geophys J Int* 199(3):1910–1918. <https://doi.org/10.1093/gji/ggu365>
- Hofmann C, Courtillot V, Feraud G, Rochette P, Yirgu G, Ketefo E, Pik R (1997) Timing of the Ethiopian flood basalt event and implications for plume birth and global change. *Nature* 389(6653):838–841
- Hyndman R (1979) Poisson's ratio in the oceanic crust—a review. *Tectonophysics* 59(1–4):321–333
- Illsley-Kemp F, Keir D, Bull JM, Gernon TM, Ebinger C, Ayele A, Hammond JO, Kendall JM, Goitom B, Belachew M (2018) Seismicity during continental breakup in the Red Sea Rift of northern Afar. *J Geophys Res Solid Earth* 123(3):2345–2362
- IRIS D (2012) Data services products: SWS-DBS shear-wave splitting databases
- Joffe S, Garfunkel Z (1987) Plate kinematics of the circum Red Sea—a re-evaluation. *Tectonophysics* 141(1–3):5–22
- Kandilarov A, Mjelde R, Flueh E, Pedersen RB (2015) V_p/V_s -ratios and anisotropy on the northern Jan Mayen ridge, north Atlantic, determined from Ocean Bottom Seismic data. *Polar Sci* 9(3):293–310
- Keir D, Belachew M, Ebinger C, Kendall JM, Hammond JO, Stuart G, Ayele A, Rowland J (2011) Mapping the evolving strain field during continental breakup from crustal anisotropy in the Afar depression. *Nat Commun* 2(1):1–7
- Kennett BL, Engdahl E, Buland R (1995) Constraints on seismic velocities in the Earth from traveltimes. *Geophys J Int* 122(1):108–124

- Kind R, Yuan X, Mechie J, Sodoudi F (2015) Structure of the upper mantle in the north-western and central united states from us arrays-receiver functions. *Solid Earth* 6(3):957–970. <https://doi.org/10.5194/se-6-957-2015>
- Kodaira S, Bellenberg M, Iwasaki T, Kanazawa T, Hirschleber HB, Shimamura H (1996) Vp/Vs ratio structure of the Lofoten continental margin, northern Norway, and its geological implications. *Geophys J Int* 124(3):724–740. <https://doi.org/10.1111/j.1365-246X.1996.tb05634.x>
- Koptev A, Gerya T, Calais E, Leroy S, Burrov E (2018) Afar triple junction triggered by plume-assisted bi-directional continental break-up. *Sci Rep* 8(1):1–7
- Korostelev F, Weemstra C, Leroy S, Boschi L, Keir D, Ren Y, Molinari I, Ahmed A, Stuart GW, Rolandone F et al (2015) Magmatism on rift flanks: insights from ambient noise phase velocity in Afar region. *Geophys Res Lett* 42(7):2179–2188
- Koulakov IY (2007) Structure of the Afar and Tanzania plumes based on the regional tomography using ISC data. In: *Doklady earth sciences*, Citeseer, vol 417, p 1287
- Kumar U, Legendre CP (2021) STADIUM-Py: Python command-line interface for automated receiver functions and shear-wave splitting measurements. Zenodo. <https://doi.org/10.5281/zenodo.4686103>
- Kusky TM, Toraman E, Raharimahefa T, Rasozanamparany C (2010) Active tectonics of the Alaotra-Ankay graben system, Madagascar: possible extension of the Somalian-African diffusive plate boundary? *Gondwana Res* 18(2–3):274–294
- Langston CA (1979) Structure under Mount Rainier, Washington, inferred from teleseismic body waves. *J Geophys Res Solid Earth* 84(B9):4749–4762
- Legendre C (2013) Shear wave velocity model of the upper mantle beneath Europe and surroundings. Doctoral Thesis, Ruhr-Universität Bochum, Universitätsbibliothek
- Legendre C, Zhao L, Deschamps F, Chen QF (2016) Layered anisotropy within the crust and lithospheric mantle beneath the Sea of Japan. *J Asian Earth Sci* 128:181–195
- Legendre C, Tseng T, Zhao L (2020) Surface-wave phase-velocity maps of the Anatolia region (Turkey) from ambient noise tomography. *J Asian Earth Sci* 193:104322
- Legendre CP, Tseng TL, Chen YN, Huang TY, Gung YC, Karakhanyan A, Huang BS (2017) Complex deformation in the Caucasus region revealed by ambient noise seismic tomography. *Tectonophysics* 712:208–220
- Maguire R, Ritsema J, Goes S (2018) Evidence of subduction-related thermal and compositional heterogeneity below the United States from transition zone receiver functions. *Geophys Res Lett* 45(17):8913–8922
- McClusky S, Reilinger R, Ogubazghi G, Amleson A, Healeb B, Vernant P, Sholan J, Fisseha S, Asfaw L, Bendick R et al (2010) Kinematics of the southern Red Sea-Afar triple junction and implications for Plate dynamics. *Geophys Res Lett* 37(5):L05301
- McQuarrie N, Stock J, Verdel C, Wernicke B (2003) Cenozoic evolution of Neotethys and implications for the causes of plate motions. *Geophys Res Lett* 30(20):2036
- Mège D, Korme T (2004) Dyke swarm emplacement in the Ethiopian Large Igneous Province: not only a matter of stress. *J Volcanol Geotherm Res* 132(4):283–310
- Megies T, Beyreuther M, Barsch R, Krischer L, Wassermann J (2011) Obspy-what can it do for data centers and observatories? *Ann Geophys* 54(1):47–58
- Mohr P (1970) The Afar triple junction and sea-floor spreading. *J Geophys Res* 75(35):7340–7352
- Musacchio G, Mooney WD, Luetgert JH, Christensen NI (1997) Composition of the crust in the Grenville and Appalachian provinces of North America inferred from Vp/Vs ratios. *J Geophys Res Solid Earth* 102(B7):15225–15241
- Ni S, Tan E, Gurnis M, Helmberger D (2002) Sharp sides to the African Superplume. *Science* 296(5574):1850–1852
- Obrebski M, Kiselev S, Vinnik L, Montagner JP (2010) Anisotropic stratification beneath Africa from joint inversion of SKS and P receiver functions. *J Geophys Res Solid Earth* 115(B9):B09313
- Reed CA, Almadani S, Gao SS, Elsheikh AA, Cherie S, Abdelsalam MG, Thurmond AK, Liu KH (2014) Receiver function constraints on crustal seismic velocities and partial melting beneath the Red Sea rift and adjacent regions, Afar depression. *J Geophys Res Solid Earth* 119(3):2138–2152
- Reilinger R, McClusky S (2011) Nubia-Arabia-Eurasia plate motions and the dynamics of mediterranean and middle east tectonics. *Geophys J Int* 186(3):971–979
- Rychert CA, Hammond JO, Harmon N, Kendall JM, Keir D, Ebinger C, Bastow ID, Ayele A, Belachew M, Stuart G (2012) Volcanism in the Afar rift sustained by decompression melting with minimal plume influence. *Nat Geosci* 5(6):406–409
- Savage MK (1999) Seismic anisotropy and mantle deformation: what have we learned from shear wave splitting? *Rev Geophys* 37(1):65–106. <https://doi.org/10.1029/98RG02075>
- Schilling JG, Kingsley RH, Hanan BB, McCully BL (1992) Nd-Sr-Pb isotopic variations along the gulf of aden: Evidence for Afar mantle plume-continental lithosphere interaction. *J Geophys Res Solid Earth* 97(B7):10,927–10,966
- Sebai A, Stutzmann E, Montagner JP, Sicilia D, Beucler E (2006) Anisotropic structure of the African upper mantle from Rayleigh and love wave tomography. *Phys Earth Planet Inter* 155(1–2):48–62
- Sicilia D, Montagner JP, Cara M, Stutzmann E, Debayle E, Lépine JC, Lévêque JJ, Beucler E, Sebai A, Roult G et al (2008) Upper mantle structure of shear-waves velocities and stratification of anisotropy in the Afar hotspot region. *Tectonophysics* 462(1–4):164–177
- Silver PG (1996) Seismic anisotropy beneath the continents: probing the depths of geology. *Annu Rev Earth Planet Sci* 24(1):385–432
- Simmons NA, Forte AM, Grand SP (2007) Thermochemical structure and dynamics of the African Superplume. *Geophys Res Lett* 34(2):L02301
- Tesaro M, Kaban MK, Petrunin AG, El Khrepy S, Al-Arifi N (2018) Strength and elastic thickness variations in the Arabian plate: a combination of temperature, composition and strain rates of the lithosphere. *Tectonophysics* 746:398–411
- Tesfaye S, Harding DJ, Kusky TM (2003) Early continental breakup boundary and migration of the Afar triple junction, Ethiopia. *GSA Bull* 115(9):1053–1067
- Thompson D, Hammond JO, Kendall JM, Stuart G, Helffrich G, Keir D, Ayele A, Goitom B (2015) Hydrous upwelling across the Mantle Transition Zone beneath the Afar triple junction. *Geochem Geophys Geosyst* 16(3):834–846
- Trabant C, Hutko AR, Bahavar M, Karstens R, Ahern T, Aster R (2012) Data products at the IRIS DMC: stepping stones for research and other applications. *Seismol Res Lett* 83(5):846–854
- Venzke E (2013) Global volcanism program, 2013. *Volcanoes of the world*, v 4.5, 2
- Walker KT, Bokelmann GH, Klemperer SL, Nyblade A, Walker K, Bokelmann G, Klemperer S, Nyblade A (2005) Shear wave splitting around hotspots: evidence for upwelling-related mantle flow? *Spec Pap Geol Soc Am* 388:171
- Walpersdorf A, Vigny C, Ruegg JC, Huchon P, Asfaw LM, Kirbasha SA (1999) 5 years of GPS observations of the Afar triple junction area. *J Geodyn* 28(2):225–236
- Walpole J, Wookey J, Masters G, Kendall J (2014) A uniformly processed data set of SKS shear wave splitting measurements: a global investigation of upper mantle anisotropy beneath seismic stations. *Geochem Geophys Geosyst* 15(5):1991–2010
- Wignall PB (2001) Large igneous provinces and mass extinctions. *Earth-Sci Rev* 53(1–2):1–33
- Wüstefeld A, Bokelmann G (2007) Null detection in shear-wave splitting measurements. *Bull Seismol Soc Am* 97(4):1204–1211
- Wüstefeld A, Bokelmann G, Barruol G, Montagner JP (2009) Identifying global seismic anisotropy patterns by correlating shear-wave splitting and surface-wave data. *Phys Earth Planet Inter* 176(3–4):198–212
- Zandt G, Ammon CJ (1995) Continental crust composition constrained by measurements of crustal Poisson's ratio. *Nature* 374(6518):152–154
- Zhu L, Kanamori H (2000) Moho depth variation in southern California from teleseismic receiver functions. *J Geophys Res Solid Earth* 105(B2):2969–2980

Publisher's Note

Springer Nature remains neutral with regard to jurisdictional claims in published maps and institutional affiliations.